

# Change Detection Using Airborne LiDAR: Applications to Earthquakes

Aravindhan K. Krishnan, Edwin Nissen, Srikanth Saripalli,  
Ramon Arrowsmith, and Alejandro Hinojosa-Corona

**Abstract.** We present a method for determining 3-dimensional, local ground displacements caused by an earthquake. The technique requires pre- and post-earthquake point cloud datasets, such as those collected using airborne Light Detection and Ranging (Lidar). This problem is formulated as a point cloud registration problem in which the full point cloud is divided into smaller windows, for which the local displacement that best restores the post-earthquake point cloud onto its pre-earthquake equivalent must be found. We investigate how to identify the size of window to be considered for registration. We then present an information theoretic approach that classifies whether a region contains an earthquake fault. These methods are first validated on simulated earthquake datasets, for which the input displacement field is known, and then tested on a real earthquake. We show results and error analyses for a variety of different window sizes, as well as results for our fault detection algorithm.

**Keywords:** Change detection, Airborne systems, Registration, ICP.

## 1 Introduction

Continental earthquakes occur within wide networks of faults which pose a serious hazard to local populations, yet most of these faults remain unmapped

---

Aravindhan K. Krishnan · Edwin Nissen · Srikanth Saripalli · Ramon Arrowsmith  
Autonomous Systems Technologies Research and Integration Laboratory  
Arizona State University, USA  
e-mail: [aravindhan.krishnan@asu.edu](mailto:aravindhan.krishnan@asu.edu)  
<http://robotics.asu.edu>

Alejandro Hinojosa-Corona  
Division de Ciencias de la Tierra, CICESE, Mexico  
e-mail: [alhinc@cicese.mx](mailto:alhinc@cicese.mx)  
<http://www.cicese.mx>

or poorly documented [4]. To better understand the tectonics of these regions and to help constrain the likely timing and magnitude of future seismicity, it is crucial to map earthquake-related surface deformation, and from this, calculate the distribution and sense of slip on the causative faulting. Satellite radar interferometry (InSAR) has proved a powerful method for measuring far-field earthquake displacements, but the technique often breaks down close to the fault rupture (due to ground disruption) and is insensitive to North-South motions (because of its viewing geometry). Sub-pixel correlation of optical images helps solve these problems, but can only determine lateral displacements, leaving the important vertical component unresolved.

Sub-meter resolution topographic data derived from airborne Lidar offer huge potential for complementing these existing techniques by providing 3-dimensional, near-fault surface displacements and fault slip. Such datasets are rapidly becoming widespread; in California, for instance, Lidar data have been collected along most of the key active faults over the past decade, including the full length of the onshore San Andreas Fault [2, 7]. Were a future earthquake to occur on one of these faults, a repeat Lidar scan of the fault would enable differential analysis of dense, pre- and post-earthquake topographic data. The 4 April 2010 El Mayor-Cucapah earthquake ( $M_w$  7.2) in northern Mexico is currently the only earthquake rupture with both pre- and post-event Lidar coverage. A simple differencing of gridded Digital Elevation Models (DEMs) generated from these point clouds revealed spectacular images of surface faulting and complex off-fault deformation [6]. However, these maps do not account for lateral displacements and so cannot be directly equated to any single component of the 3-D displacement field.

Computing the full 3-D surface displacements following an earthquake could potentially revolutionize our understanding of rupturing processes and would greatly aid research on faulting and tectonics in earthquake-prone regions. The objectives of this work are to devise a method to compute full 3-D displacements from pre- and post-earthquake Lidar datasets, and in doing so identify the causative faulting and its sense and magnitude of slip.

## 2 Problem Statement

The problem can be formulated as follows. Given pre- and post-earthquake Lidar point clouds (each containing a scattered distribution of points), find the 3-dimensional displacement (with rotation and translation components) that has best shifted the post-earthquake point cloud from its pre-earthquake equivalent. These shifts will vary spatially, depending on the distance to the fault, the sense and magnitude of slip and secondary effects such as landsliding. For this reason, the area must be divided into separate windows and the best local transformation identified for each one. To complicate matters, post-event windows which contain surface faulting will not be related by a rigid body transformation to their pre-event equivalents.

A few things must be considered in this problem statement. Firstly, how do we decide upon an appropriate window size for splitting the data? Secondly, without any prior knowledge, how do we identify whether a particular window contains the fault, or lies away from the fault and has been shifted?

### 3 Data Description

We began our experiments using a synthetic earthquake dataset, before moving on to real earthquake displacements. The synthetic post-earthquake dataset was generated by adding displacements of known magnitude and sense to a real point cloud (the ‘target cloud’), to be tested against another, unaltered point cloud representing the pre-earthquake ground surface (the ‘source cloud’). This way, we were able to identify an approach which best reproduced the known input displacements. We used publicly available “B4” Lidar data [2] covering a  $\sim 2 \times 2$  km section of the San Andreas Fault (SAF) near Coachella, CA, collected on five separate, parallel flight lines with  $\sim 50\%$  overlap between adjacent swaths. In the realistic case, pre- and post-earthquake datasets would utilize different Lidar scan lines, so we split the original dataset by flight line, using the 1st, 3rd and 5th swaths for the source cloud and adding synthetic earthquake displacements to the 2nd and 4th flight lines for the target cloud. Both datasets have average point cloud densities of  $\sim 2$  points/m<sup>2</sup>. Our synthetic fault strikes North-West through the center of the target cloud, close to the real surface trace of the SAF. To simulate a vertical, right-lateral rupture, we displaced points North-East of the fault 2 m towards the South-East, and displaced points South-West of the fault 2 m towards the North-West. To evaluate our ability to detect vertical motions, we also raised points on the North-East of the fault by 1 m. After investigating the synthetic case, we go on to test the method using real pre- and post-earthquake data from part of El Mayor-Cucapah earthquake rupture in Mexico [6]. Here, the pre- and post-earthquake point cloud densities are on average 0.013 points/m<sup>2</sup> and  $\sim 9$  points/m<sup>2</sup>, respectively.

### 4 Algorithm

We use the Iterative Closest Point (ICP) algorithm [1] with a point to plane metric [8] for point cloud alignment. ICP operates by finding the corresponding point  $q_i$  in the target cloud for every point  $p_i$  in the source cloud, and determines the rigid body transformation that minimizes the distances between these points. It is an iterative process where the correspondences and the errors are computed at every iteration and the rigid body transformation is applied to the source cloud repeatedly until it aligns with the target cloud. With the point to plane error metric, the objective is to minimize the distance between the source point ( $p_i$ ) and the tangent plane at the corresponding target point ( $q_i$ ). The error metric can be written as follows

$$E = \sum_i \| (\phi p_i - q_i) \cdot n_i \|^2 \quad (1)$$

where  $\phi$  is the rigid body transformation that minimizes the error metric and  $n_i$  is the normal to the tangent plane at  $q_i$ . The transformation matrix consists of a translation component and a rotation component.  $\phi = T(t_x, t_y, t_z) \cdot R(\alpha, \beta, \gamma)$ . A linear approximation [5] can be made to the rotation matrix where  $\theta \approx 0$  and the new transformation matrix is of the form below.

$$\phi = \begin{pmatrix} 1 & -\gamma & \beta & t_x \\ \gamma & 1 & -\alpha & t_y \\ -\beta & \alpha & 1 & t_z \\ 0 & 0 & 0 & 1 \end{pmatrix} \quad (2)$$

We explain how the computed transformation is validated in section 6.

## 5 Approach

We began by choosing an arbitrary window size in the source cloud (e.g. 200 m  $\times$  200 m). For each of these windows, the corresponding window in the target data is identified based on  $x$  and  $y$  coordinates. This target window is then enlarged (e.g. by 10%) such that the displacements that we are trying to quantify are fully accommodated. Next, we computed the rigid body transformation between the source and target windows using the ICP algorithm. This window is split into four smaller windows of equal size and the rigid body transformation is computed on every child window. The transformation is validated after each split (explained in section 6) and the associated error computed. Based on the differences in error after consecutive splits, we decide whether further splitting is necessary. We verified experimentally that we cannot have small errors for very small window sizes ( $\sim 10$  m) given the point cloud densities and input displacements. An analysis of this error indicates when to stop splitting.

After running ICP using a good window size, each window is then considered for a fault analysis. The curvature of the local surface is computed at every point in the transformed source windows (obtained by applying the computed transformation on the source window i.e.  $\phi p_i$ ) and target windows ( $q_i$ ) and the curvature distribution is estimated by assigning the curvature computed at each point to different bins of an histogram (ranging from *max-curvature* to *min-curvature*) and then computing the probability mass function from this histogram. If there is no rigid body transformation (in case of windows containing the fault) the source and target curvature distributions will not be the same. An information theoretic measure is used to detect this inconsistency in the curvature distributions. The information gain between the transformed source cloud ( $X$ ) and the target cloud ( $Y$ ) is given by

$$I(X; Y) = H(X) + H(Y) - H(X, Y) \quad (3)$$

where  $H$  is the entropy of the curvature distribution.  $H(X, Y)$  is computed on the curvature distribution of the merged clouds  $X$  and  $Y$ . When the right window size is used on regions related by a rigid body transformation, the information gain should be maximum. If the estimated transformation is sub-optimal (i.e. if ICP converges to a local minima) or if the considered region is not related by a rigid body transformation (in the case of windows containing faulting) the information gain should be minimal. Hence thresholding based on information gain highlights which windows contain the fault, along with a few false positives where ICP results may be different from the ground truth. It is important to choose the right window size. If a window containing the fault is too large, then points lying away from the fault will dominate the curvature distribution and the fault detection mechanism will be affected.

Various non-rigid body transformation methods are available in medical imaging literature [3] and can be considered for this problem. Our goal is not only to get the best alignment possible, but also to identify regions containing the fault. A rigid body transformation estimation followed by a transformation validation achieves both the objectives, whereas the second objective is not met by non-rigid body transformation estimation methods.

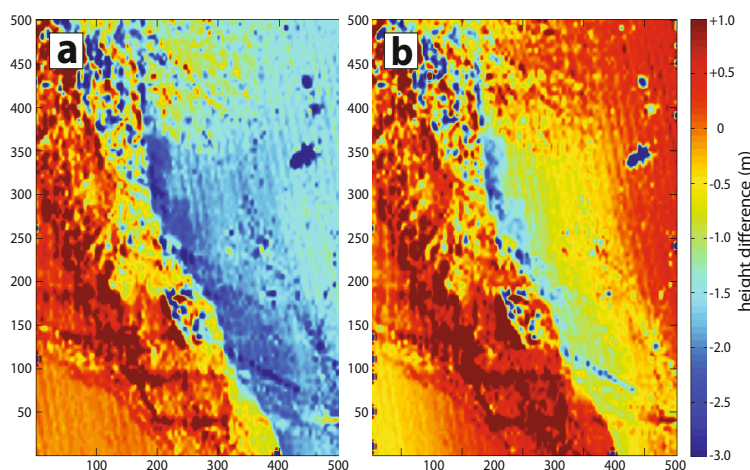


**Fig. 1** (a) Height difference map of the Mexico earthquake, before global ICP, with  $x$  and  $y$  coordinates in meters. Height changes across the fault are clear. (b) Height difference map after global ICP, with height differences reduced.

## 6 Transformation Validation

We validate the transformations by randomly choosing  $N$  points per iteration in the transformed source window ( $\phi p_i$ ) and finding the closest point in the target window ( $q_i$ ). The error for the  $k^{th}$  iteration is computed as  $E_k = \sum_i \|\phi p_i - q_i\|^2$  and the standard deviation of this error is calculated over  $k$  iterations. For a good alignment the standard deviation should be minimal. Figure 7 shows the standard deviation of errors for different window sizes. It can be seen that the standard deviation increases gradually as the windows become smaller (part *a* of the figure shows plots for window sizes of 75 m, 50 m and 25 m). However, at a particular point (for our data, a window size of 10 m) the standard deviation jumps markedly, as shown in part *b* (note the difference in  $y$ -axis scales between *a* and *b*). If this happens, it is because the computed transformation for that window is wrong. To discard these invalid transformations, we use a thresholding based on the change in standard deviation as a stopping criteria for window splitting (whereby the standard deviation should not exceed  $1/m$  times that of the previous step).

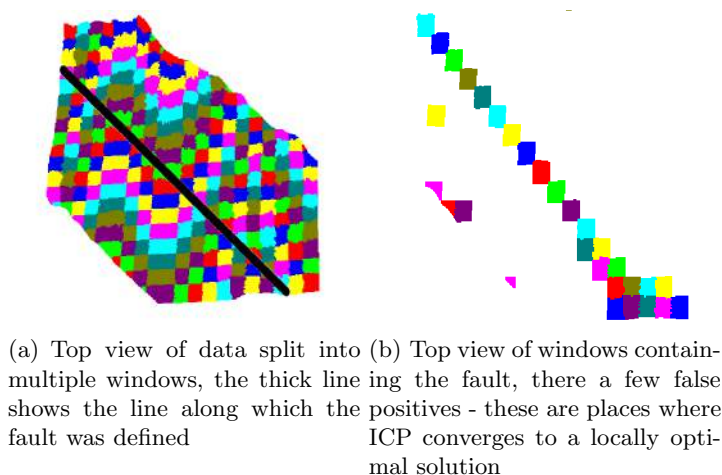


**Fig. 2** Window split and fault detection

## 7 Results

Figure 1a shows a simple height differencing of the raw Mexico earthquake data, with clear positive height changes West of the fault and negative changes East of the fault. After a global registration, these height differences are reduced with similar height changes on both sides, as seen by the red shading in Figure 1b. This is because ICP has minimized the least square error over the entire point cloud, including both those regions that contain

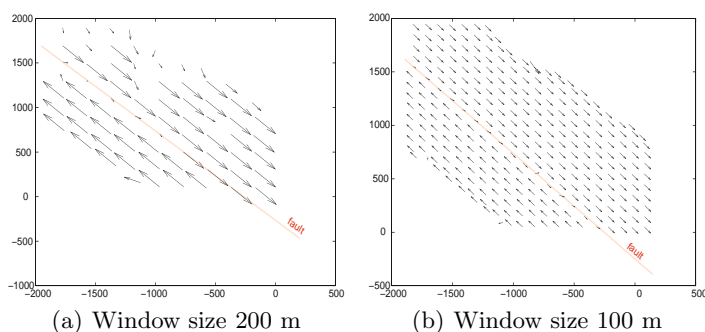


**Fig. 3** Displacement vectors for different window sizes. The approximate length of the displacement vectors is 2 m. Notice the change in vector directions on both sides of the fault.  $x$  and  $y$  values are in meters.

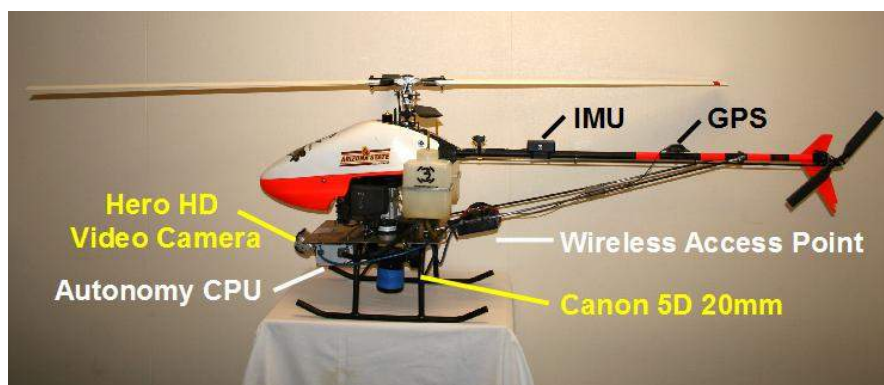


**Fig. 4** Our Autonomous Helicopter platform

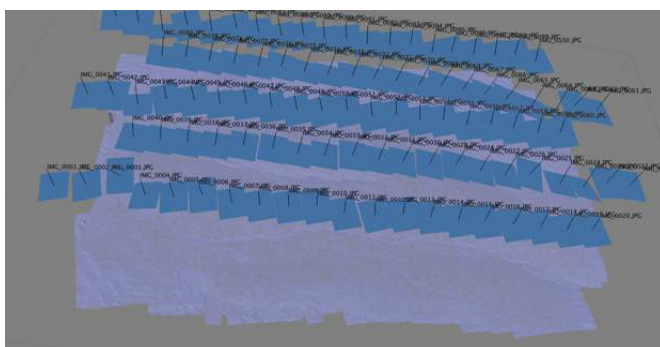
the fault and those that are displaced. The alignment occurring as a result of this least square minimization is not sensitive to the local displacements that we are trying to quantify, and hence a global registration is not suitable for this problem.

Figure 2(a) shows the data split up into multiple, randomly coloured windows with the thick black line showing the synthetic fault line, either side of which artificial displacements were added (as described in section 3).

Figures 3(a) and 3(b) show the displacement vectors ( $\sim 2$ m in length) obtained for different window sizes for the synthetic earthquake dataset. The change in the direction of the displacement vectors either side of the fault (shown by the red line) are obvious. However, the displacement vectors for windows along the fault are inconsistent. These are windows that are not related by a rigid body transformation and ICP finds the transformation



**Fig. 5** 3D model of Las Cruces test site (400 x 100 m) generated from UAV flights at approximately 50m AGL



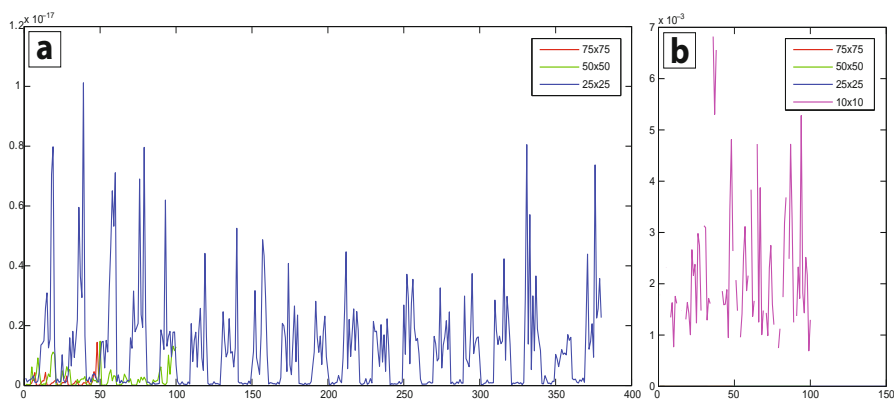
**Fig. 6** 3D model of Las Cruces test site with UAV position and attitude inferred from photogrammetric process

that minimizes the least squares error. Reducing window sizes beyond this point did not satisfy our transformation validation criteria and hence further splitting of windows was stopped.

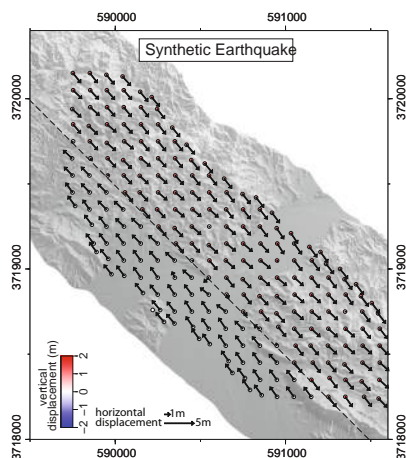
Figure 2(b) shows the results of our fault detection method, which filters out windows based on information gain as described in section 5. Compared to figure 2(a), only those windows which fall below the information gain threshold are now shown, including a North-West trending sequence of windows along the fault. In addition, there are a few false positives, mostly along the edges where window splitting has left few data points in one of the datasets. We hypothesise that ICP converges to a local minima in these windows.

Figure 7 shows the standard deviation plots discussed in the previous section. Figure 8 shows the displacements calculated for the synthetic earthquake overlaid on the actual topography (we used a DEM derived from publicly available “B4” Lidar data). Black arrows are horizontal displacements and coloured circles denote vertical displacements. The differences in these displacements are clear on either side of the fault. Finally results on a real





**Fig. 7** Standard deviations by window number, for different window sizes. (a) shows the plot for window sizes of 75 m (red), 50 m (green) and 25 m (blue). In (b), we also plot standard deviations for window size of 10 m (purple), with an enlarged  $y$ -axis scale such that the standard deviations for the 75 m, 50 m and 25 m window sizes are barely visible. There is a huge increase in standard deviation when the window size is reduced from 25 m to 10 m, suggesting that window splitting should be stopped at 25 m.



**Fig. 8** Results for the simulated earthquake. Horizontal displacements (black arrows) and vertical displacements (coloured circles) can clearly be seen to change markedly either side of the fault.  $x$  and  $y$  axes show UTM Zone 11 coordinates, in meters.

earthquake dataset (for the 2010 Mexico earthquake) can be seen in Figure 9. Again, differences in the horizontal and vertical displacements on opposing sides of the fault are clear.

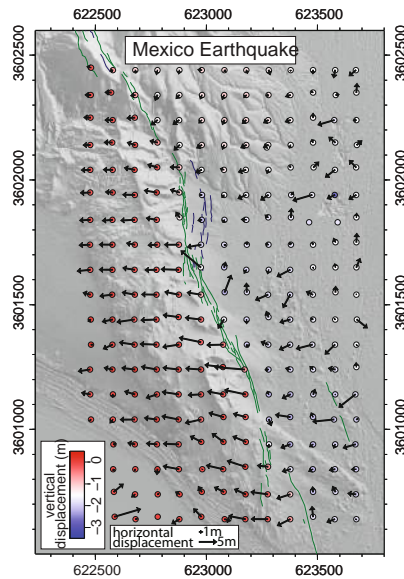


**Fig. 9** Results for the real earthquake. The thin lines show the earthquake surface faulting, as observed by geologists, with E-facing scarps in green and W-facing scarps in blue. Again, the horizontal and vertical displacements clearly change markedly across the fault.  $x$  and  $y$  axes show UTM Zone 11 coordinates, in meters.

## 8 Conclusions and Future Work

We have demonstrated a technique for determining local displacements caused by an earthquake. Our technique uses a windowing approach to determine the correct displacements and an information theoretic approach for determining the regions where these local displacements are present. We have demonstrated the efficacy and accuracy of our technique on datasets collected using airborne lidar. We are able to discern displacements of 1.4 m over an area of  $2 \times 2$  km in our synthetic earthquake experiments and around 1 m over  $2 \times 2$  km in the real earthquake experiment. Currently our technique depends on the pre and post LIDAR data obtained using expensive airborne LIDAR. We plan on using the pre data obtained from airborne LIDAR but post data obtained using Structure from Motion techniques. We propose to use an autonomous helicopter equipped with a downward looking Canon 5D as our platform for obtaining these post point clouds. Our autonomous helicopter is shown in Figure 4. This platform has been outfitted with a vibration isolating camera mount to which the main SFM camera (a Canon 5D) is attached. Figure 5 shows a typical 3D terrain model obtained from our UAV. Figure 6 shows the attitude and position of the UAV calculated using SFM, as the images were taken. This was generated in Las Cruces,

New Mexico, for an area approximately 400 x 100 m. The model has a resolution of 10cm/pixel and an accuracy of 20 cm. This has been determined using pre-surveyed points using a Total Station. In the future we plan on using such dense 3D models created from SFM techniques as our post point clouds. Using such models combined with registration techniques will enable us to determine local displacements accurately. We plan on demonstrating this in the near future.

**Acknowledgements.** The B4 project was lead by Ohio State University, the US Geological Survey and the National Center for Airborne Laser Mapping (NCALM), with support from the National Science Foundation (NSF). We thank all these groups — as well as others involved in supporting the project, including the many landowners along the fault — for the exceptional quality of their dataset and for making it publicly available through the OpenTopography portal. We are very grateful to the Instituto Nacional de Estadística y Geografía (INEGI) for giving us access to the Mexico pre-earthquake dataset. The Mexico post-earthquake data were collected by NCALM through an NSF RAPID award to Mike Oksin (UCD) and Ramon Arrowsmith. We would like to further extend our thanks to all these (and other) collaborators for many fruitful discussions on this exciting new topic of research. OpenTopography and NCALM are supported by the Earth Sciences Instrumentation and Facilities Program at the US National Science Foundation.

## References

1. Besl, P.J., McKay, N.D.: A method for registration of 3-d shapes. *IEEE Trans. Pattern Anal. Mach. Intell.* 14, 239–256 (1992)
2. Bevis, M., Hudnut, K., Sanchez, R., Toth, C., Grejner-Brzezinska, D., Kendrick, E., Caccamise, D., Raleigh, D., Zhou, H., Shan, S., Shindle, W., Yong, A., Harvey, J., Borsa, A., Ayoub, F., Shrestha, R., Carter, B., Sartori, M., Phillips, D., Coloma, F.: The B4 Project: Scanning the San Andreas and San Jacinto Fault Zones. In: *AGU Fall Meeting Abstracts*, pp. H34–B01 (December 2005)
3. Crum, T., Hartkens, W.R., Hill, D.L.G.: Non rigid Image Registration: theory and practice. *British Journal of Radiology* (2004)
4. England, P., Jackson, J.: Uncharted seismic risk. *Nature Geoscience* 4, 348–349 (2011)
5. Low, K.-L.: Linear least squares optimization for point-to-plane ICP surface registration. Technical Report TR04-004
6. Oskin, M.E., Arrowsmith, J.R., Hinojosa-Corona, A., Elliott, A.J., Fletcher, J.M., Fielding, E.J., Gold, P.O., Garcia, J.J.G., Hudnut, K.W., Liu-Zeng, J., Teran, O.J.: Near-Field Deformation from the El Mayor-Cucapah Earthquake Revealed by Differential LIDAR. *Science* 335, 702–705 (2012)
7. Prentice, C.S., Crosby, C.J., Whitehill, C.S., Arrowsmith, J.R., Furlong, K.P., Phillips, D.A.: Illuminating Northern California's Active Faults. *Eos Trans. AGU* 90, 55–55 (2009)
8. Rusinkiewicz, S., Levoy, M.: Efficient variants of the ICP algorithm. In: *International Conference on 3-D Digital Imaging and Modeling* (2001)